Reprinted from

journal of nuclear materials

Journal of Nuclear Materials 228 (1996) 184–200

Hot-isostatic pressing of U–10Zr by a coupled grain boundary diffusion and creep cavitation mechanism [1]

S.M. McDeavitt *, A.A. Solomon

School of Nuclear Engineering, Purdue University, West Lafayette, IN 47907, USA

Received 12 April 1995; accepted 27 October 1995

ELSEVIER

JOURNAL OF NUCLEAR MATERIALS

Scope

The Journal of Nuclear Materials publishes high quality papers in materials research relevant to nuclear fission and fusion reactor technologies, and in closely related aspects of materials science and engineering. Both original research and critical review papers covering experimental, theoretical, and computational aspects of either fundamental or applied nature are welcome. The breadth of the field is such that a wide range of processes and properties is of interest to the readership, spanning atomic lattice defects, microstructures, thermodynamics, corrosion, and mechanical and physical properties, for example. The following list, which is not exhaustive, describes topics appropriate to the Journal.

- Fission reactor materials, including fuels, cladding, core structures, pressure vessels, moderator and control components; fission product behavior.
- Materials aspects of the fabrication and reprocessing of fuels.
- Performance of nuclear waste materials, glasses and ceramics, immobilization of wastes.
- Fusion reactor materials, including first walls, blankets, insulators, and magnets.
- Neutron radiation effects in materials, including defects, microstructures, transmutations, phase changes, and macroscopic properties.
- Interactions of plasmas, ion beams, electron beams and electromagnetic radiation with materials.

Abstracted/indexed in:

Aluminium Industry Abstracts: Chemical Abstracts: Current Contents: Engineering, Computing and Technology: Current Contents: Physical, Chemical and Earth Sciences: EI Compendex Plus: Engineered Materials Abstracts: Engineering Index: INSPEC: Metals Abstracts: Physics Briefs.

Subscription Information 1996

Volumes 228–239 of Journal of Nuclear Materials (ISSN 0022-3115) are scheduled for publication. Prices are available from the publishers upon request. Subscriptions are accepted on a prepaid basis only. Issues are sent by SAL (Surface Air Lifted) mail wherever this service is available. Airmail rates are available upon request. Please address all enquiries regarding orders and subscriptions to:

Elsevier Science BV
Order Fulfilment Department
PO Box 211, 1000 AE Amsterdam
The Netherlands
Tel.: +31-20 485 3642; Fax: +31-20 485 3598.

Claims for issues not received should be made within six months of our publication (mailing) date. If not, they cannot be honoured free of charge.

US mailing notice – Journal of Nuclear Materials (ISSN 0022-3115) is published monthly, except semimonthly in April, June, September, October, November and December, by Elsevier Science BV, Molenwerf 1, PO Box 211, 1000 AE Amsterdam, The Netherlands. The annual subscription price in the USA is US$ 4215 (valid in North, Central and South America only), including air speed delivery. Second class postage paid at Jamaica, NY 11431.
USA Postmasters: Send changes to Journal of Nuclear Materials, Publications Expediting, Inc., 200 Meacham Avenue, Elmont, NY 11003. Airfreight and mailing in the USA by Publications Expediting.

♾ The paper used in this publication meets the requirements of ANSI/NISO Z39.48-1992 (Permanence of Paper).

Printed in The Netherlands

North-Holland, an imprint of Elsevier Science

ELSEVIER

Journal of Nuclear Materials 228 (1996) 184–200

journal of nuclear materials

Hot-isostatic pressing of U–10Zr by a coupled grain boundary diffusion and creep cavitation mechanism [1]

S.M. McDeavitt *, A.A. Solomon

School of Nuclear Engineering, Purdue University, West Lafayette, IN 47907, USA

Received 12 April 1995; accepted 27 October 1995

Abstract

To investigate the mechanical response of porous and swelling metallic fuel to cladding restraint, specimens of U–10 wt% Zr were prepared from $UH_3 + ZrH_2$ and U + Zr powders. Specimens were sintered under argon to entrap gas and simulate fission gas bubbles and contained different amounts of rigid precipitates resulting from impurities in the starting powders. Hot-isostatic pressing (HIP) was performed at 600°C ($\alpha + \delta$-phase) and 700°C (γ-phase). The phenomenon of HIP is related to grain boundary diffusion and creep cavitation mechanisms for cavity growth during creep. Densification was not detected at 600°C, but occurred readily at 700°C. The driving force dependence at 700°C ($n = 3.7 \pm 0.5$) and observed loading/unloading transients are consistent with a creep-controlled HIP mechanism. The activation energy (187 ± 10 kJ/mol) agrees with a reported value for grain boundary diffusion of uranium in γ-U, consistent with a grain boundary diffusion-controlled mechanism. The overall mechanism thus appears to be coupled grain boundary diffusion and creep cavitation. The relevance to in-reactor densification under external pressure or contact stress is also discussed.

1. Introduction

Uranium with 10 wt% zirconium (U–10Zr) is a metallic nuclear fuel that was used in Experimental Breeder Reactor-II (EBR-II) and as part of the Integral Fast Reactor (IFR) program at Argonne National Laboratory [1]. Metallic nuclear fuels were previously rejected for high-burnup fast reactors due, in part, to fission gas-induced swelling and anisotropic irradiation growth, which caused fuel-cladding mechanical interaction (FCMI) and cladding rupture at low burnup under normal operating conditions [1]. To accommodate swelling and gas release, fuel pins for the IFR were designed with a large sodium-filled gap between the fuel and the cladding and an enlarged gas plenum that allowed fuel swelling and fission gas release before fuel–cladding contact [1].

After cladding contact, which occurs at 1–2 at.% burnup [1], the fuel must densify to accommodate additional fuel swelling from retained fission products. Therefore, the compressibility of the highly porous fuel is important because it represents the fuel's ability to relax the contact stresses that arise during continued fuel swelling. Since the target burnup of the IFR was greater than 20 at.% [1], this situation was significant over the majority of the fuel's lifetime. The problem of FCMI becomes unavoidable when fuel swelling is constrained by low-swelling cladding materials, and FCMI-induced strains were observed at low burnup in the U–10Zr fuel rods used in EBR-II [2]. Another complication would occur at high burnup when solid fission products (primarily lanthanides) precipitate in available porosity, especially in outer regions of the

* Corresponding author. Present address: Argonne National Laboratory. Chemical Technology Division, 9700 South Cass Avenue, Argonne, IL 60439, USA. Tel.: +1-708 252 4308; fax: +1-708 252 9917; e-mail: sean_mcdeavitt@qmgate.anl.gov.

[1] This work was supported by the Office of Reactor Engineering, US Department of Energy, under Contract No. DE-FG02-88ER12814.

SSDI 0022-3115(95)00220-0

fuel cross section [2], impairing the fuel's compressibility. In addition, a rapid temperature rise during a reactor transient may also generate contact stresses because of different thermal expansion in the fuel and cladding and increases in fission gas bubble pressure.

To address these issues, hot-isostatic pressing (HIP) experiments have been carried out on unirradiated, porous U–10Zr. The technique used [3] has been employed to study swelling and HIP in UO_2 [4–6] and in Ni [7], ZnO [8], and Al_2O_3 [9]. Since no other primary data are available for U–10Zr, the purpose of the present experiments was to identify and quantify the rate-controlling HIP mechanism in pure, unirradiated U–10Zr in the $\alpha + \delta$- and γ-phase fields. The $\alpha + \delta$-phase (α-uranium plus UZr_2) is stable below 617°C, and the γ phase (body-centered cubic solid solution) is stable above 693°C [2].

2. Theoretical background

Hot-isostatic pressing and swelling of porous material at elevated temperatures are stress- and temperature-dependent phenomena. To a first approximation, they are opposing directions of the same process if they do not involve irreversible fracture. It has been shown that models developed for diffusional creep cavitation under uniaxial stress are even more appropriate for HIP and swelling where the stress is hydrostatic, and excellent agreement between theory and experiment is obtained if the internal pore pressure and pore surface energy are included [10]. Comprehensive reviews of creep cavitation mechanisms are available [10,11].

Creep cavitation mechanisms may be broadly classified into two categories: (1) grain boundary diffusion controlled cavitation and (2) creep-controlled cavitation. A model for diffusion-controlled cavitation was formulated and refined by several authors [12–18]; the rate-controlling mechanism is the stress-directed motion of vacancies from grain boundaries to cavity surfaces via grain boundary diffusion. Creep-controlled cavitation models have also been developed by several authors [19–21]; the rate-controlling mechanism is the creep of material surrounding the cavity when diffusional fluxes are assumed unable to relax the applied tensile stress because either grain boundary diffusion is limited or cavities are not on the grain boundary. In a general situation, however, diffusion- and creep-controlled cavitation mechanisms operate simultaneously,

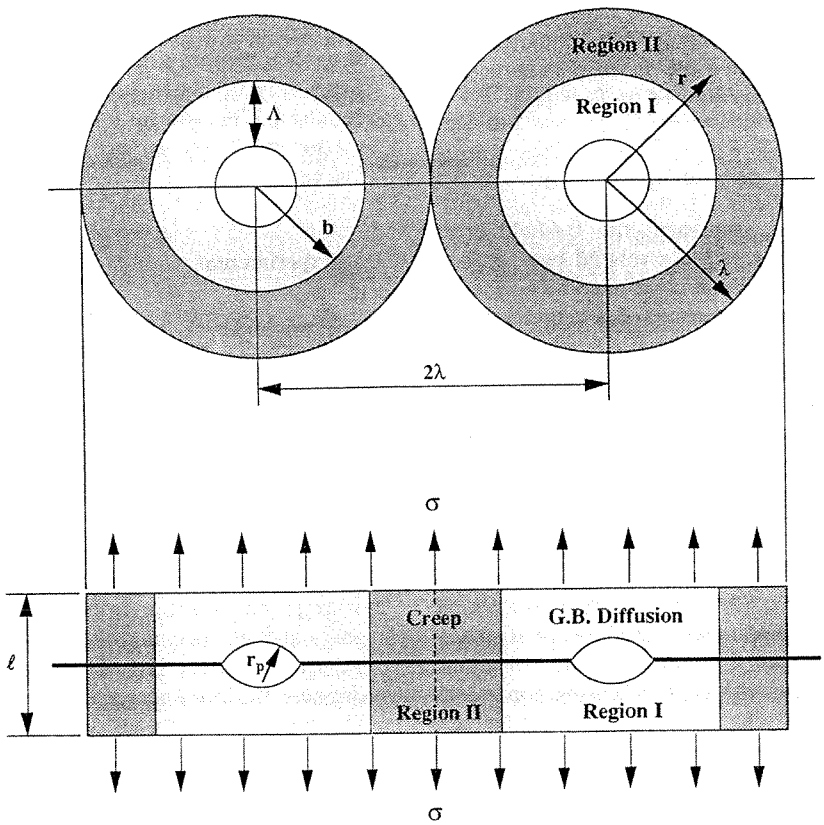

Fig. 1. Geometry of the Beere–Speight model [19] for coupled grain boundary diffusion and creep cavitation.

and total cavitation may be modeled through coupling both mechanisms [19,22–26].

The Speight and Beere [15] model, concluded to best represent diffusion-controlled cavitation [22], is written as

$$\left(\frac{dv}{dt}\right)_{gb} = \frac{2\pi\Omega D_b \delta_b}{kTf(r_p/\lambda)}\left[\sigma - p + \frac{2\gamma}{r_p}\right], \quad (1)$$

which is the volume rate of change (dv/dt) for an individual cavity on a grain boundary normal to an applied tensile stress, σ. The subscript gb denotes the grain boundary diffusion mechanism. In the first term on the right-hand side, Ω is the atomic volume, D_b is the grain boundary diffusion coefficient, δ_b is the boundary width, k is Boltzmann's constant, and T is the temperature. Also, the factor $f(r_p/\lambda)$ is a complex geometric structure function related to the pore size-to-spacing ratio, where λ is half the distance between cavity centers [15]. The bracketed term represents the diffusional driving force, F; for HIP or swelling, $F = P - p + 2\gamma/r_p$, where P is the external isostatic pressure, p is the internal cavity or pore pressure, γ is the surface tension, and r_p is the cavity radius of curvature [10].

Following the development of the diffusion-controlled model, significant progress has been made toward incorporating creep flow into cavitation models. Needleman and Rice [24] coupled both mechanisms numerically, and established the use of the characteristic diffusion length, Λ, as defined by Rice [27]:

$$\Lambda = \left(\frac{D_b \delta_b \Omega \sigma_\infty}{kT\dot{\varepsilon}_\infty}\right)^{1/3}. \quad (2)$$

The terms σ_∞ and $\dot{\varepsilon}_\infty$ represent the far-field creep stress and creep rate, which are related by $\dot{\varepsilon}_\infty = B\sigma_\infty^n$, where B and n are empirical constants.

Beere and Speight [19] presented a cylindrical unit cell (Fig. 1) that is centered around a single cavity and divided into two regions. Region I represents that portion of the grain boundary next to the cavity where the diffusion-controlled mechanism operates. Region II represents that portion of the grain boundary between cavities where grain boundary diffusion is assumed to be negligible. Chen and Argon [22] improved on this concept by noting that the radial dimension of Region I should be equivalent to the characteristic diffusion length, Λ (Eq. (2)), and they derived a simple equation for the coupled model based on the displacement induced in Region I by the deposition of atoms. The calculated results using the Chen–Argon model matched very well [22] the numerical result of Needleman and Rice [24], but this was determined to be fortuitous since the assumed mechanical equilibrium conditions were inappropriate [26].

The form of the Chen–Argon model is identical to Eq. (1) without the surface tension term except for the replacement of the cavity half spacing, λ, in the structure function by a new parameter, $b = r_p + \Lambda$, which represents the radius of Region I. This difference is very significant because of the strong stress dependence of Λ (Eq. (2)). The coupled cavitation rate therefore, has a non-linear dependence on the driving force, F, whereas the diffusion-controlled mechanism (Eq. (1)) has a linear dependence on F. Martinez and Nix [25] extended the Chen–Argon model to include the effect of the cavity surface tension, or capillarity. Schneibel and Martinez [26] later pointed out problems with the Chen–Argon/Martinez–Nix model which result in a discontinuity in the grain boundary stress at the boundary between Regions I and II. The discontinuity is negligible when Λ is large, but it becomes increasingly serious as the diffusion zone shrinks and plastic hole growth dominates. Schneibel and Martinez [26] derived a cavity growth rate expression which is more physically accurate and is also strongly dependent upon Λ, and thus non-linear with respect to F.

These models require the assumption of uniform cavity sizes and spacings so that a single, representative volume element can be analyzed. While such models may capture some of the basic physics, important interactions are omitted if pore sizes and spacings can vary. If pore sizes vary, diffusional fluxes from cavity to cavity cause coarsening [28], which can greatly increase the creep rupture time. For non-equilibrium cavities or pores ($F \neq 0$), elastic interactions can give rise to cavity repulsion [28], and for variable spacings, plastic deformation may play an increasing role as pore spacing increases [29].

3. Experimental

Two types of U–10Zr specimens were prepared from powder mixtures. One type was derived from uranium hydride (UH_3) and zirconium hydride (ZrH_2) powders, and the other type was derived from uranium metal microspheres and zirconium metal powder. The powders are pyrophoric, requiring an inert atmosphere, so samples were prepared inside a glovebox under purified argon. The general procedure for all specimens was to press the powders in a stainless steel punch and die, sinter the green pellet in the presence of argon gas in order to entrap gas in grain boundary pores at high specimen density, and raise the ambient pressure to induce HIP. The trapped gas is designed to simulate the presence of fission gas in irradiated fuel. The processing methods developed are described elsewhere [30,31], but a brief summary is presented here.

Green pellets were positioned vertically between two tungsten slugs and inserted into a tungsten pressure vessel that was sealed inside the glovebox and

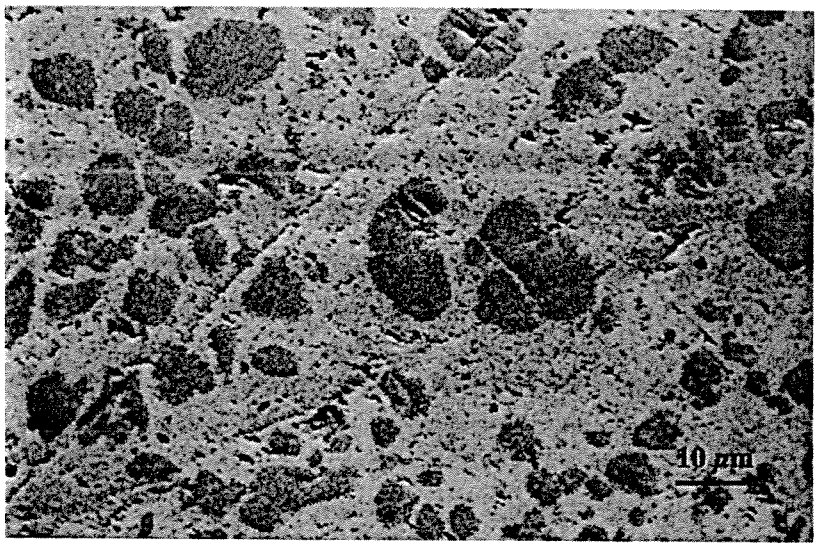

Fig. 2. Scanning electron microscope image of hydride-derived U–10Zr sintered 24 h at 1100°C.

removed to a high-pressure, high-temperature sintering system [3,30]. A molybdenum rod resting on top of the upper tungsten slug transmitted changes in specimen length to a linear variable differential transducer (LVDT) above the hot zone of the furnace. The vessel was connected to a high-pressure/vacuum system that can supply oxygen-gettered argon gas up to 31 MPa (4500 psi) or, alternatively, can subject the specimens to ~1 Pa (~10^{-2} Torr) vacuum. Specimen dimensions and green density were measured prior to sintering.

3.1. Hydride-derived specimens

Hydride powders (UH_3 [2] and ZrH_2 [3]) were used because of their fine particle size, compactibility, and low decomposition temperatures under vacuum. Specimens were generated by mixing the powders with an alumina mortar and pestle and then compacting the mixture at 550 MPa to yield a cylindrical pellet (0.7 cm in diameter and ~0.8 cm long with a density of ~60% TD). The pellets were then sintered at 1100°C for 24 h. After hydride decomposition, the metal density was only ~42% TD. However, even with the low relative green density, final densities of ~93% TD with complete alloying were achieved, as determined by energy dispersive X-ray (EDAX) analysis.

Sintering was carried out in a tungsten pressure vessel [3], and the sample was heated under vacuum to the sintering temperature of 1100°C in 1 h. On the basis of observed pressure transients resulting from the evolution of hydrogen during heating, it was established that UH_3 decomposed between 250 and 450°C, and ZrH_2 decomposed between 600 and 900°C [30]. After hydride decomposition at ~900°C, purified argon (< 10 ppm oxygen) was introduced into the system at 1.7 MPa to provide an ambient pressure. By the time the specimen temperature reached 1100°C, the density was typically ~70% TD, and the specimen porosity was still open, thus enabling gas entrapment.

The microstructure of the sintered hydride-derived specimens (Fig. 2) shows a globular second phase that occupies 25 vol.% of the material. The EDAX analysis indicated only zirconium in these phases, but scanning auger microscopy revealed the presence of significant quantities of carbon, nitrogen, and oxygen in the globular phases. Phases of this type are observed in cast IFR fuel rods and are reported to be zirconium with the impurities (C, N, and O) in interstitial solid solution [2]. In an effort to characterize the source of the contamination, we tracked the microstructural evolution of the impurity phase through the sintering process [30], and we concluded that the starting UH_3 powder was the primary source of contamination.

3.2. Metal-derived specimens

The uranium metal spheres [4] used were much larger than the particles of uranium hydride powder (~177

[2] Courtesy of B. Lambdin. Oak Ridge National Laboratory.
[3] A.D. Mackay, Inc.

[4] Nuclear Metals, Inc.

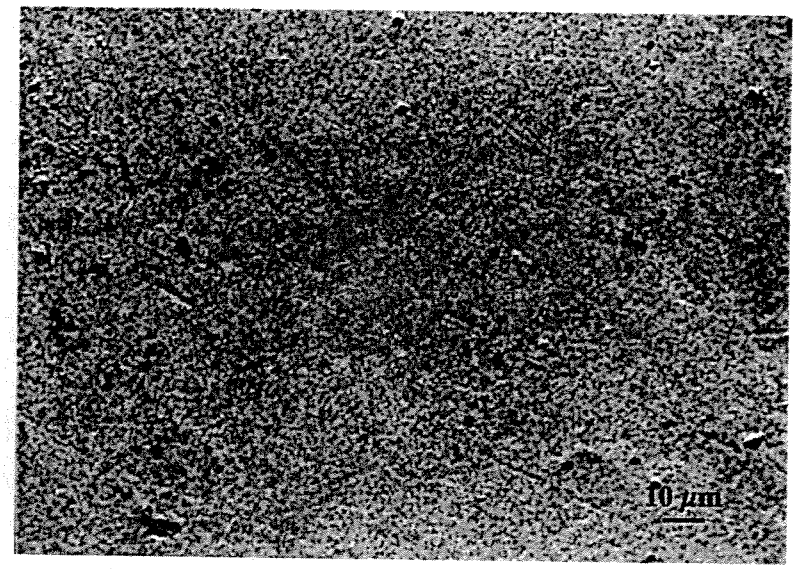

Fig. 3. Scanning electron microscope image of metal-derived U–10Zr sintered 6 h at 1200°C.

μm versus ~ 1 to 5 μm), so sintering was less efficient, and a significantly higher green density was required. The spheres also had a surface oxide layer that would act as a barrier to interdiffusion during sintering. This layer was removed, following Lloyd and Williams [32], by washing with a 20% nitric acid bath until the metal surface had high reflectivity [30]. The washed powder was rinsed with water and ethyl alcohol and then dried in the glovebox by evaporation.

The clean uranium and zirconium [5] metal powders were mixed in the sample die and compressed at 1100 MPa, forming a pellet of 80% TD. The compaction pressure was twice that used for the hydride-derived samples because it was necessary for the pure zirconium to plastically flow around the uranium spheres to form a strong specimen. After compaction, the specimens were transferred from the glovebox to the tungsten pressure vessel, which was evacuated and backfilled with purified argon several times between 100 and 200°C as the vessel temperature was being raised. The system was then pressurized with 3.5 MPa of argon and heated to 1100°C in 1 h.

In contrast to the hydride-derived powders, no observable shrinkage occurred until the temperature exceeded ~ 1000°C, when the samples began to shrink rapidly. Rothman [33] reported that interdiffusion between uranium and zirconium does not readily occur until both elements are in their body-centered cubic, high-temperature phase ($T > 863$°C). Since the specimen temperature lagged the furnace temperature by as much as 150°C during the heating to 1100°C, the present observations are consistent with Rothman's.

After 6 h at 1100°C, sintering stopped and the alloy was well mixed [30], but the porosity did not fully close. Because of this, the process was modified so that the specimens were held at 1100°C for 30 min, and then the temperature was raised to 1200°C for 6 h. Specimens could not be taken directly to 1200°C because it is above the melting point of pure uranium (1132°C), and time must be allowed for diffusional alloying. With this method, specimens were sintered to ~ 91% TD with closed, gas-filled porosity. The metal-derived specimens had fewer zirconium impurity particles (typically below 5 vol.%) than the hydride-derived specimens (compare Fig. 3 with Fig. 2).

3.3. Hot-isostatic pressing procedure

Following sintering, the temperature was lowered and held at 700°C (γ-phase U–10Zr) or 600°C (α + δ-phase U–10Zr) for 1 h to thermally stabilize the system and verify that no further detectable densification occurred. The external pressure was then raised (in less than 10 s) to initiate HIP. Strain rates were calculated from data on change in length versus time generated by the LVDT signal as recorded on a strip chart. Pressure changes of various magnitudes were used to investigate the pressure/driving force dependence of the HIP process, as discussed in the next section.

[5] Cerac. Inc.

4. Results of hot-isostatic pressing experiments

4.1. Hot-isostatic pressing results

Several HIP experiments were performed on the hydride-derived specimens at 700°C (γ-phase) with ambient pressure increases (ΔP) of 3.5, 6.9, 10.5, 13.8, and 20.7 MPa. The strain rate versus time results are presented in Fig. 4. Some of the transients in Fig. 4 (6.9 and 10.5 MPa) have been truncated for clarity because of perturbations made to measure the HIP activation energy and driving force dependence; the full perturbed transients are described later (Figs. 9–11). The specimens densified from 93% TD to 95–97% TD, depending on the pressure conditions.

For each experiment, Fig. 4 shows an initial linear portion (log scale) during which most of the HIP strain occurs, followed by a dramatic drop-off in the HIP strain rate. Multiple experiments were completed with $\Delta P = 6.9$, 10.5, and 13.8 MPa, and the strain rates were very reproducible. For tests with $\Delta P = 3.5$, 6.9, 10.5, and 13.8 MPa, the initial HIP strain rate decreased with time as

$$\dot{\varepsilon}_L \approx t^{-0.32}, \tag{3}$$

where the time exponent, −0.32, is the mean slope of the linear portion (log-scale) of the HIP strain rate curves (Fig. 4), excluding the 20.7 MPa transient. This relationship is similar to the time-dependent behavior observed in previous *swelling* experiments on Ni [7] and ZnO [8], in which a time dependence of $t^{-1/3}$ was observed. It is also in fair agreement with the theoretical time dependence predicted for swelling controlled by grain boundary diffusion when the internal pore pressure dominates the driving force ($t^{-2/5}$) [10]. In the experiment with $\Delta P = 20.7$ MPa, however, the material behaved differently, with the strain rate exhibiting a time dependence of

$$\dot{\varepsilon}_L \approx t^{-0.74}. \tag{4}$$

The results of HIP experiments at 700°C (γ-phase) for metal-derived specimens are presented in Fig. 5, with some of the transients truncated for clarity, as before. Two regions of time-dependent behavior are again evident, but in contrast to the hydride-derived specimens, the initial HIP rate of the metal-derived specimens decreased over all driving forces with a time dependence of

$$\dot{\varepsilon}_L \approx t^{-0.13}. \tag{5}$$

To investigate the behavior of the α + δ two-phase alloy, which corresponds to the phases present near the IFR fuel surface [1,2], two HIP experiments were attempted with the metal-derived samples at 600°C with $\Delta P = 17.3$ MPa. No HIP strains were detectable in either specimen at this temperature. Prior to HIP, one specimen was annealed at 600°C for 6 h and the other

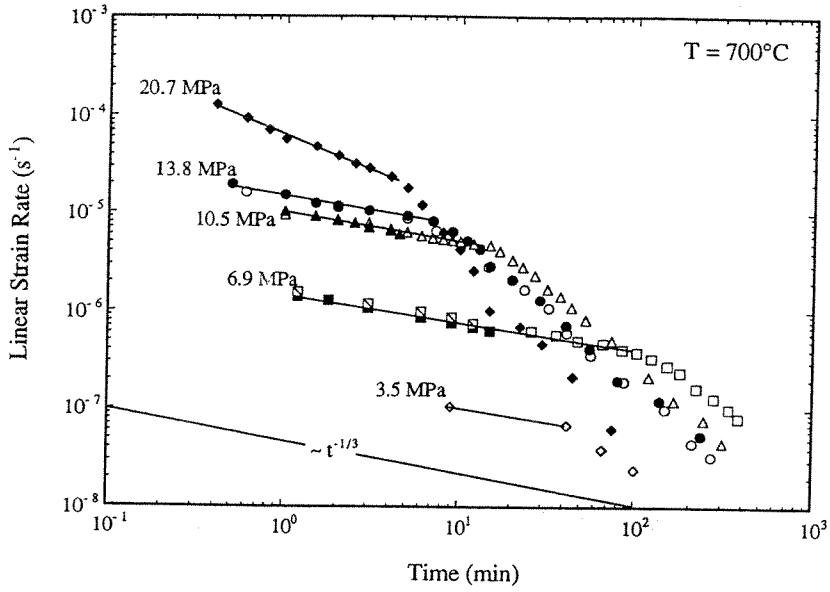

Fig. 4. HIP results at 700°C for hydride-derived U–10Zr specimens. Points on same curve with different symbols represent repetitions of the same experimental conditions.

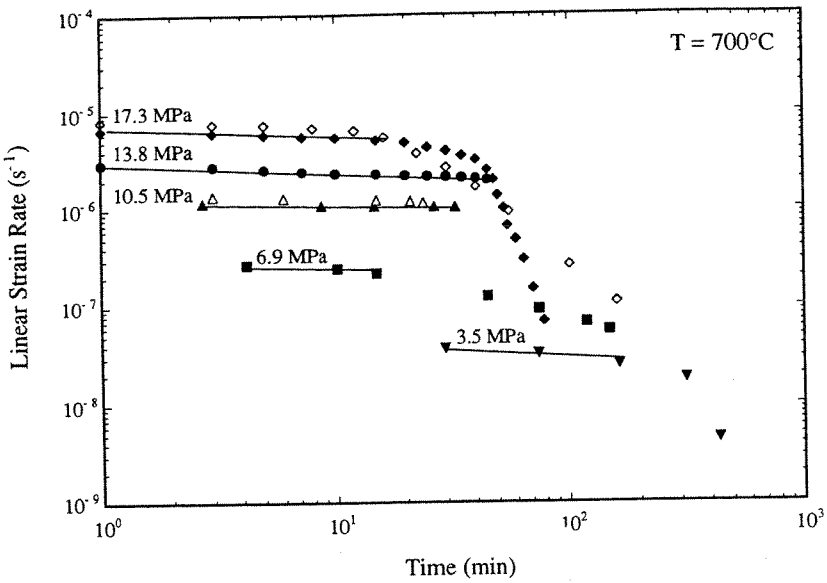

Fig. 5. HIP results at 700°C for metal-derived U–10Zr specimens. Points on same curve with different symbols represent repetitions of the same experimental conditions.

for 50 h to generate an equilibrium microstructure. It is reported that "no more than 48 h" is required to generate the two-phase structure at this temperature [34], but the δ-phase was not detected by scanning electron microscope analysis of either sample. To verify that the pressure driving forces and closed porosity were similar to those in the 700°C experiments, the temperature of the first sample was raised to 700°C one hour after the initial ΔP. The sample hot-pressed very rapidly, indicating that the porosity was closed and filled with gas.

4.2. Specimen microstructures

For the results of these HIP experiments to be compared with theoretical models, microstructural information is required from both types of specimens. The porosity distribution and the impurity particle size

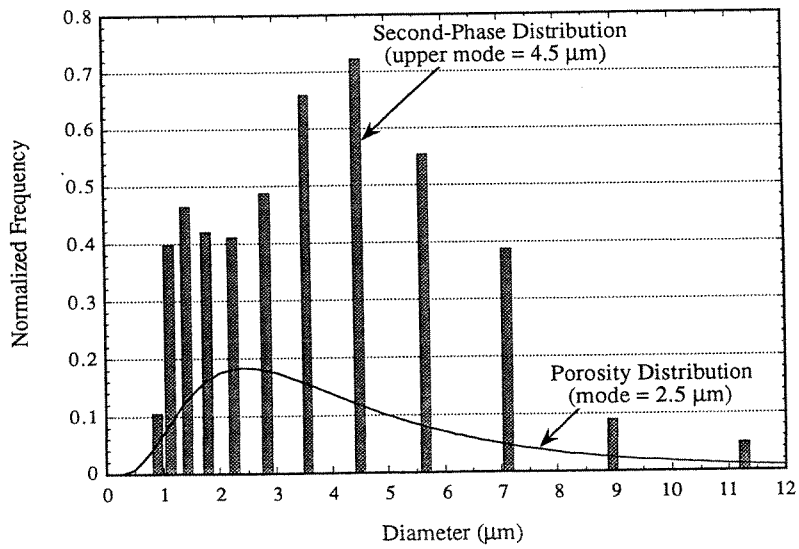

Fig. 6. Normalized porosity and second-phase particle size distributions in hydride-derived U–10Zr.

distribution were measured by using *NIH Image v1.43* to analyze digital images of post-HIP samples captured from a high-resolution video camera through an optical microscope. Grain sizes were evaluated by standard lineal analysis on polished surfaces etched with 49% nitric acid, 49% lactic acid, and 2% hydrofluoric acid.

For the hydride-derived materials, five areas with 1260 pores and two areas with 660 second-phase particles were analyzed. For the metal-derived materials, two areas with 250 pores and four areas with 480 second-phase particles were analyzed. For all cases, the measured two-dimensional distributions were translated by standard calculation methods into three-dimensional distributions [31]. The normalized frequency distributions for the hot-pressed pore size and the zirconium second-phase particle size in the hydride- and metal-derived materials are shown in Figs. 6 and 7.

The porosity in both types of samples had log-normal distributions with modal pore diameters of 2.5 ± 0.1 and 1.7 ± 0.1 μm for the hydride- and metal-derived samples, respectively. The hydride-derived porosity had a calculated number density of 9.3×10^{14} m^{-3} and a volume fraction of 6.4%, and the metal-derived porosity had a calculated number density of 5.5×10^{14} m^{-3} and a volume fraction of 4.2%. As noted earlier, the creep cavitation models assume spherical cavities or cavities with a circular cross section in the grain boundary. The pores observed in the U–10Zr samples were generally round and free from sharp, crack-like edges. Therefore, the assumption of spherical porosity is valid as a first approximation of the pore shape.

The second-phase particle size distributions for both materials are bimodal, with an upper mode of 4.5 μm for both materials. However, the hydride-derived material has a much higher particle density (5.0×10^{15} m^{-3} versus 3.9×10^{14} m^{-3}) and volume fraction (25% versus 4.8%). The metal-derived specimens have fewer impurities, so the zirconium content in solution should be higher. This expectation was verified by EDAX analysis, which showed that the matrix composition averaged over several specimens [31] was only 4.7 wt% Zr (11.5 at.%) for the hydride-derived samples but 9.4 wt% Zr (21.3 at.%) for the metal-derived samples.

By using lineal analysis to measure the mean intercept length and assuming the grain shape to be a space-filling tetrakaidecahedron (following Mendelson [35]), we found the average grain size to be 34 ± 5 and 114 ± 10 μm for the hydride- and metal-derived specimens, respectively. On the basis of the grain size and number densities, the pore spacings (2λ in Fig. 1) were calculated to be 10 and 7 μm (±10%), and the particle spacings were calculated to be 4 and 8 μm (±10%) for the hydride- and metal-derived specimens. It was assumed that all pores and particles are on grain boundaries. This assumption was validated from the etched microstructures, which had little intragranular porosity.

4.3. Deformation parameters in hot-isostatic pressing

The dependence of the HIP strain rate on the driving force and the temperature are indicators of the rate-controlling mechanism. It was reported [10] that the cavitation mechanisms discussed in Section 2 may be generally described as the product of three physical terms, given as

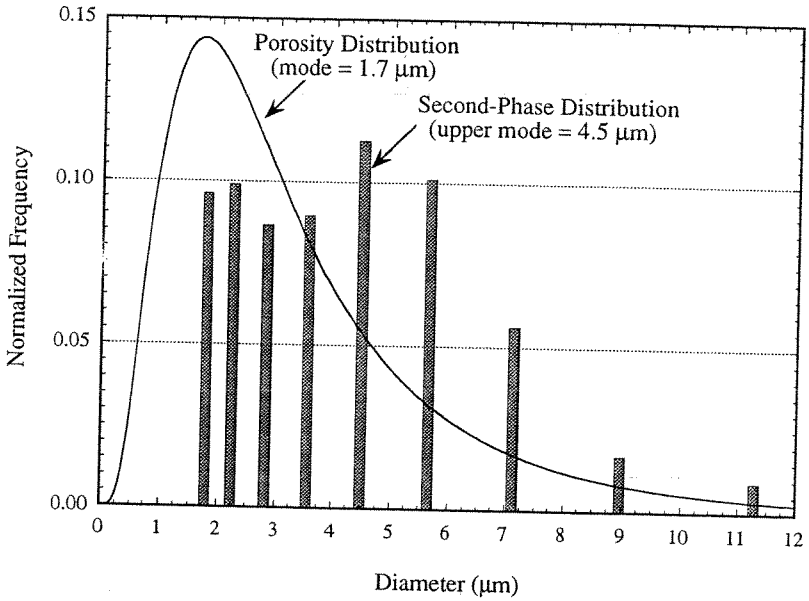

Fig. 7. Normalized porosity and second-phase particle size distributions in metal-derived U–10Zr.

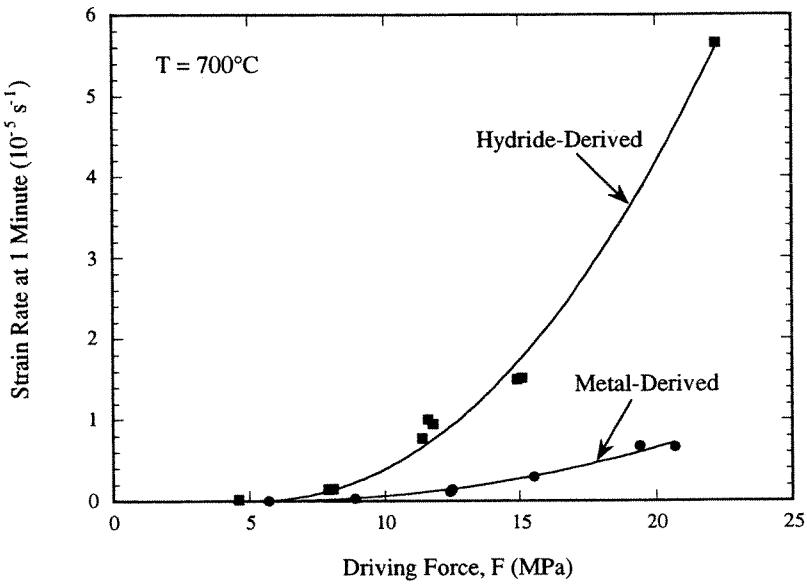

Fig. 8. Extrapolated initial HIP rates ($t = 1$ min) versus the initial driving force, showing a non-linear driving force dependence.

$$\dot{\varepsilon} = SKF^n, \tag{6}$$

where S is a temperature-independent structure term; K is kinetic term that can be represented as $K = K_0 \exp[-Q/RT]$; F is the driving force, $P - p + 2\gamma/r_p$; n is the driving force dependence of the HIP strain rate; and Q is the HIP activation energy. The values of n and Q were measured in the present experiments.

To determine n, the measured HIP strain rates shown in Figs. 4 and 5 were extrapolated in time to 1 min to compare the initial strain rates to the initial HIP driving forces. This comparison is valid at 1 min since specimens with the same sintering history would

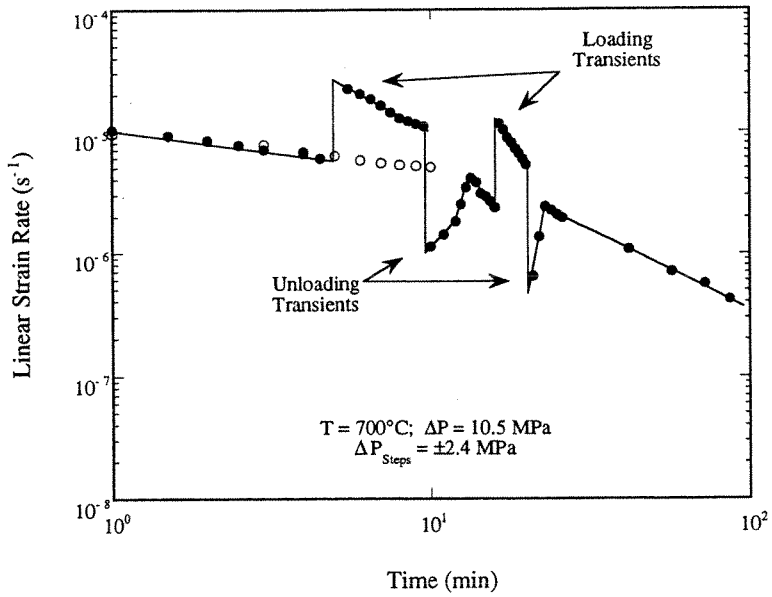

Fig. 9. Results of first perturbation experiment with hydride-derived material, showing loading/unloading transients. For reference, open symbols indicate an identical HIP transient without perturbations.

have similar initial pore structures. The initial value of F was calculated by assuming ideal gas behavior and local equilibrium ($F = 0$) after sintering. The internal pore pressure, p, at 700°C was estimated from the gas content in the pore after sintering. The U–Zr surface tension, γ, was taken as 1.5 J/m^2, given values of 1.55 and 1.40 J/m^2 at the melting temperature for liquid uranium and zirconium, respectively [31]. The estimated error in F (± 1 MPa) arises primarily from uncertainty in the surface tension.

The extrapolated strain rates are shown in Fig. 8 versus the calculated initial driving forces, which ranged between 5 and 20 MPa. The driving force dependence of the HIP strain rate is non-linear ($n \neq 1$) for both types of U–10Zr samples. Also, this comparison shows that the metal-derived specimens hot-pressed at a lower rate than the hydride-derived specimens for similar driving forces. A power-law curve fit of the data in Fig. 8 yields an n value of 3.7 ± 0.5 for *both* the hydride- and metal-derived materials.

A second, independent measure of n was generated directly from perturbations in the strain rate following small, rapid changes in the external pressure during HIP transients. Even though the pore structure slowly changes during HIP, the strain rate after the step change may be extrapolated back to the same pore structure (constant S in Eq. (6)), assuming that no other microstructural features change with stress. If a constant structure term (S) and kinetic term (K) and a variable driving force (F) are assumed, the logarithm of the differential of Eq. (6) yields

$$n = \frac{\ln(\dot{\varepsilon}_1/\dot{\varepsilon}_2)}{\ln(F_1/F_2)}, \tag{7}$$

where the subscripts 1 and 2 indicate the strain rate and driving force conditions before and after the pressure perturbations. The driving forces were estimated in the same manner as the initial driving forces with corrections for external pressure changes and pore shrinkage, which affects the internal and surface tension pressures.

Figs. 9 and 10 show examples of the HIP perturbation experiments that were performed on hydride-derived specimens. The first hydride-derived perturbation sample (Fig. 9) was hot-pressed with an initial ΔP of 10.5 MPa followed by four ΔP perturbations of ± 2.4 MPa. However, unexpectedly large loading and unloading transients exaggerated the apparent n values up to 6 to 10. Such transients are typical for dislocation-controlled processes in which a stress increase causes blocked dislocations to break free, while a stress decrease causes dislocations to become blocked until their density can be reduced by recovery [36]. The second hydride-derived perturbation sample (Fig. 10) was hot-pressed with an initial ΔP of 10.5 MPa, as before, followed by a single perturbation of +1.9 MPa. The smaller pressure perturbation was intended to minimize the loading transient, and the single step allowed the loading transient to dissipate, improving the accuracy of the strain rate extrapolation. From the data shown in Fig. 10, the driving force dependence

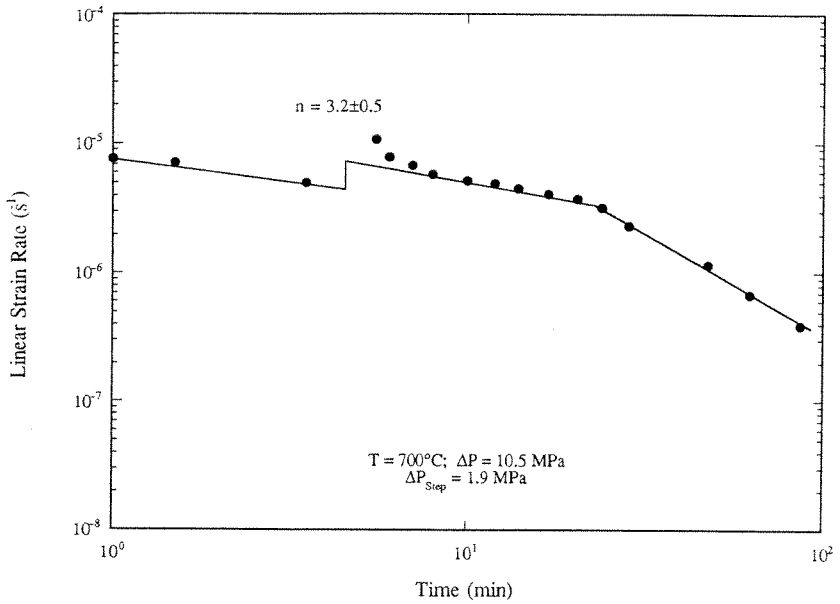

Fig. 10. Results of second perturbation experiment with hydride-derived material. A single ΔP step was used to minimize the effect of the loading transient.

was calculated to be in = 3.2 ± 0.5, which agrees well with the curve-fit n value of 3.7 ± 0.5 obtained from Fig. 8.

Similar perturbation experiments were completed on the metal-derived material. The first metal-derived perturbation sample was hot-pressed with an initial ΔP of 13.8 MPa followed by a single perturbation of +0.7 MPa, and the resulting n value was 3.5 ± 0.5. The loading transient for this experiment was much smaller in magnitude and duration than the hydride-derived transients, since the magnitude of the perturbation was smaller. Because metal-derived HIIP transients, in general, have lower rates and longer durations than hydride-derived transients, a perturbation experiment was done with an initial ΔP of 10.5 MPa followed by several increases of +1.7 MPa. However, the loading transients were unexpectedly smaller in magnitude and duration than in the hydride-derived transients. These perturbations yielded values for the driving force dependence of $n = 3.8 \pm 0.6$, 3.1 ± 0.5, and 3.2 ± 0.5, which give a mean value of 3.4 ± 0.3 for the metal-derived material. This value is in excellent agreement with the hydride-derived n value of 3.2 ± 0.5 and the curve-fit n value of 3.7 ± 0.5.

In a manner similar to that just described for n, the activation energy, Q, is calculated from the HIP strain rate changes resulting from controlled temperature perturbations. Assuming a constant structure term (S) and a variable temperature (K and F), the logarithm of the differential of Eq. (6) yields

$$Q = \frac{-R}{1/T_1 - 1/T_2}\left[\ln(\dot{\varepsilon}_1/\dot{\varepsilon}_2) - n\ln(F_1/F_2)\right] \quad (8$$

where the subscripts 1 and 2 indicate the temperature strain rate, and driving force conditions before an after the temperature perturbations. The second tern within the brackets relates to the change in the drivin force that results from the change in the interna pressure with temperature. The value of F is calcu lated as before, assuming ideal gas behavior.

A typical temperature perturbation experiment (Δ = ±25°C) is shown in Fig. 11 for a hydride-derive transient with an initial ΔP of 6.9 MPa. Similar pertur bation experiments were completed on another hy dride-derived sample and a metal-derived sample. Tak ing $n = 3$ in Eq. (8) in accordance with the curren results, we calculated activation energies of 200 ± 1 181 ± 10, and 181 ± 10 kJ/mol for the hydride-derive samples and 180 ± 10 and 182 ± 10 kJ/mol for th metal-derived sample. Taken together, these data yiel a mean HIP activation energy of 187 ± 10 kJ/mol fo U–10Zr.

5. Discussion

We had suggested earlier [30,37] that, on the basi of the models of Ashby [38] and Arzt et al. [39], a interface-controlled grain boundary diffusion mecha nism may control the rate of HIP in U–10Zr. Wit zirconium present both as a solute and as second-phas

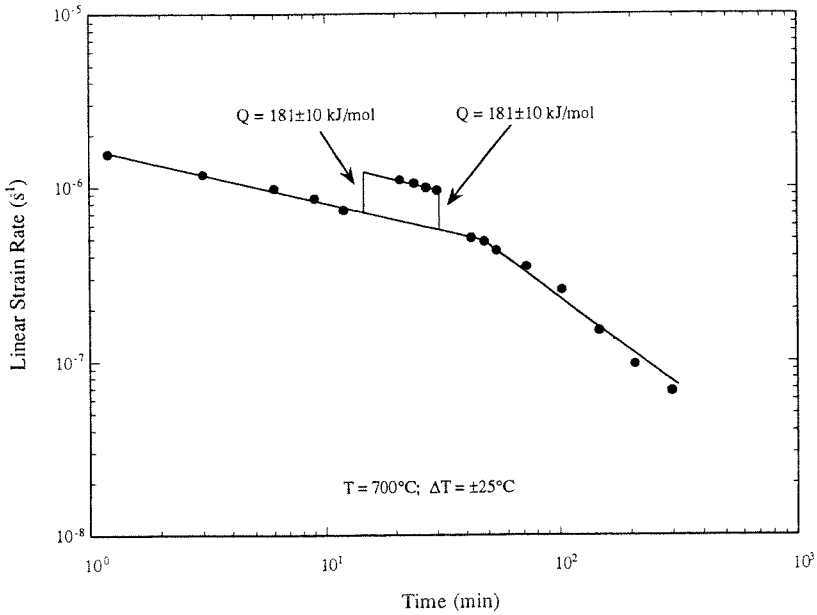

Fig. 11. Temperature perturbation experiment with hydride-derived material; ΔT steps were ±25°C.

particles, the present conditions are qualitatively consistent with such models. However, the n value predicted by these models is 2 [30], and a 'threshold' stress of ~ 5 MPa would be required to shift the present n values from 3.7 ± 0.5 down to 2. From Arzt et al. [39] and our measured microstructural data, we calculated that the maximum possible threshold stress is only 0.5 and 0.2 MPa for the hydride- and metal-derived specimens, respectively. Moreover, the activation energy for this mechanism should vary with the zirconium solute concentration (5 wt% versus 9 wt%) and the relative particle density in the boundary (25 vol.% versus 5 vol.%), but the measured activation energy is identical for both types of samples. Therefore, the interface-controlled grain boundary diffusion mechanism is now discounted as the rate-controlling HIP mechanism for the present experiments.

5.1. Diffusion- and creep-controlled mechanisms

There is no apparent difference in the measured deformation parameters n (3.7 ± 0.5) and Q (187 ± 10 kJ/mol) between the two types of U–10Zr specimens. Taken together, n and Q indicate that both types exhibit the same HIP mechanism, even though the rates are somewhat different in magnitude. For the discussions that follow, the relevant diffusion data for uranium and zirconium in uranium and U–Zr alloys [33,40] are presented in Table 1.

The expectations for n and Q are markedly different for diffusion- and creep-controlled cavitation mechanisms. A diffusion-controlled mechanism (Eq. (1)) would have $n = 1$ and Q equivalent to the activation energy for grain boundary diffusion, whereas a creep-controlled mechanism would exhibit n and Q values that are related to the creep mechanism. For dislocation creep, n is typically between 3 and 5, and the measured activation energy is the same as that for volume diffusion. The creep-controlled Q value should, therefore, depend upon the U–10Zr matrix alloy composition, as evident by the variation of Q_v reported for Zr in U–5Zr and U–10Zr (Table 1).

The measured HIP activation energy (187 ± 10 kJ/mol) is significantly higher than the reported value for volume diffusion in γ-phase U–10Zr (112 kJ/mol [33]), but is in agreement with the reported value for grain boundary diffusion of uranium in γ-phase uranium (186.6 kJ/mol [40]). Dislocation core diffusion in a creep-controlled mechanism might be used to explain an activation energy of this order, but no data are available. The activation energy for volume diffusion in a U–Zr alloy containing between 5 and 10 wt% Zr should be between 134 and 113 kJ/mol [33], but the measured value is well above that range. Considering all of this, we concluded that the only thermally activated mechanism that corresponds well with the measured HIP activation energy is grain boundary diffusion. (Typically, activation energies for grain boundary diffusion should be lower than for volume diffusion, but that is apparently not the case for uranium according to the available data [33,40]. This discrepancy was noted [40] but never explained.)

On the other hand, the measured n value of 3.7 ± 0.5 is not consistent with a diffusion-controlled mechanism. Also, the loading and unloading transients observed during pressure perturbation experiments (Figs. 9 and 10) suggest a dislocation-controlled process such as creep. Such transients were not observed in earlier HIP and swelling studies on other materials [4–9]; in those studies, the results were consistent with simple diffusional cavitation models. Taken alone, the n value and loading transients could imply a creep-controlled mechanism. However, if creep were completely controlling the HIP process, we should have observed an effect from the hard impurity phases in the hydride-derived material, but in fact that material densified faster than the purer metal-derived material.

The present observations are inconsistent with the expectations for both the diffusion-controlled and the creep-controlled processes. These inconsistencies suggest that a coupled mechanism is rate-controlling for HIP of U–10Zr under the present conditions.

5.2. Coupled mechanism

The viability of the coupled mechanism, was evaluated by estimating the characteristic diffusion length, Λ (Eq. (2)). To that end, a constitutive U–10Zr creep expression must be established. In the absence of primary creep data for U–10Zr, an approximate uniaxial creep expression.

$$\dot{\varepsilon}_c = (4 \times 10^{-10})\sigma^5 \quad s^{-1}, \tag{9}$$

Table 1
Diffusion parameters for uranium and U–Zr alloys

	γ-uranium		γU–Zr [33]	
	Grain boundary diffusion [40]	Volume diffusion [33]	Volume diffusion of Zr (5 wt% Zr)	Volume diffusion of Zr (10 wt% Zr)
$D_b\delta_b)_0$ or $(D_v)_0$ (at $T = 0$ K):	3.24×10^{-11} m^3/s	1.12×10^{-7} m^2/s	10^{-7} m^2/s	10^{-8} m^2/s
Activation energy, Q:	186.6 kJ/mol	112 kJ/mol	134 kJ/mol	113 kJ/mol

was generated [31] using a correlation for creep in metals developed by Stocker and Ashby [41] and Derby and Ashby [42] (σ in MPa). In the absence of primary data, the uncertainty of this correlation is high, but Eq. (9) was found to agree with creep data for a similar uranium alloy within an order of magnitude [31]. A second parameter that must be established for the estimation of Λ is the effective stress acting normal to the grain boundary. As a first approximation, the average stress on the grain boundary in the Beere–Speight unit cell (Fig. 1) was selected. Based on a simple force balance, the average stress on the grain boundary may be written as

$$\sigma_{av} = \frac{P\lambda^2 + (2\gamma/r_p - p)r_p^2}{(\lambda^2 - r_p^2)}. \quad (10)$$

The diffusion parameters in Table 1 for U–10Zr and the constitutive creep rate (Eq. (9)) were substituted into the expression for the characteristic diffusion length (Eq. (2)). The Λ estimate is then given by

$$\Lambda = 18.9\sigma_\infty^{-4/3} \quad \mu m \quad (11)$$

when σ_∞ is in units of MPa (Ω was taken to be 10^{-29} m^3 [31]). Using the above correlation and assuming spherical pores (i.e., r_p was taken as the modal pore radii in Section 4.2), we calculated the variation of the diffusion zone radius, b, with external HIP pressure for hydride- and metal-derived U–10Zr at the beginning of the HIP transient (Fig. 12). The pore radii (r_p) and pore half-spacings (λ) are indicated along the vertical axis for reference. These results show that a coupled mechanism is viable for both types of U–10Zr specimens between external pressures of approximately 3 and 30 MPa. Below 5 MPa, b exceeds the unit cell radius, λ, indicating that the diffusion length is large enough for diffusion-controlled cavitation to dominate at low pressure.

As the external HIP pressure is increased, b decreases until it approaches r_p. This finding indicates that the diffusion length is small and creep-controlled cavitation dominates HIP at very high pressure. When P is greater than ~20 MPa, the physical discontinuity in the Chen–Argon [22] coupled cavitation model becomes serious [26]. Since this regime is near our maximum experimental external pressure of 20.7 MPa, the Chen–Argon model, despite its physical problems, may be used to satisfactorily approximate the coupled behavior of our HIP experiments.

The Chen–Argon model [22] was converted to yield a linear HIP strain rate, given by [31]

$$(\dot{\varepsilon}_L)_{cp} = \frac{2\pi}{3}\frac{N_v\Omega D_b\delta_b}{kTf(r_p/b)}\left[P - p + \frac{2\gamma}{r_p}\right], \quad (12$$

where N_v is the cavity density. Fig. 13 shows the initial HIP rates calculated using the coupled model, as well as the initial experimental HIP rate data (from Fig. 8). The figure shows a good agreement between model predictions and the measured data; the close agreement should be considered fortuitous at best, because of the assumptions made in the estimation of Λ and the inherent physical problems in the model. The most significant result is that the predicted stress dependence varies from $n = 1$ up to $n = 5$ as the diffusion

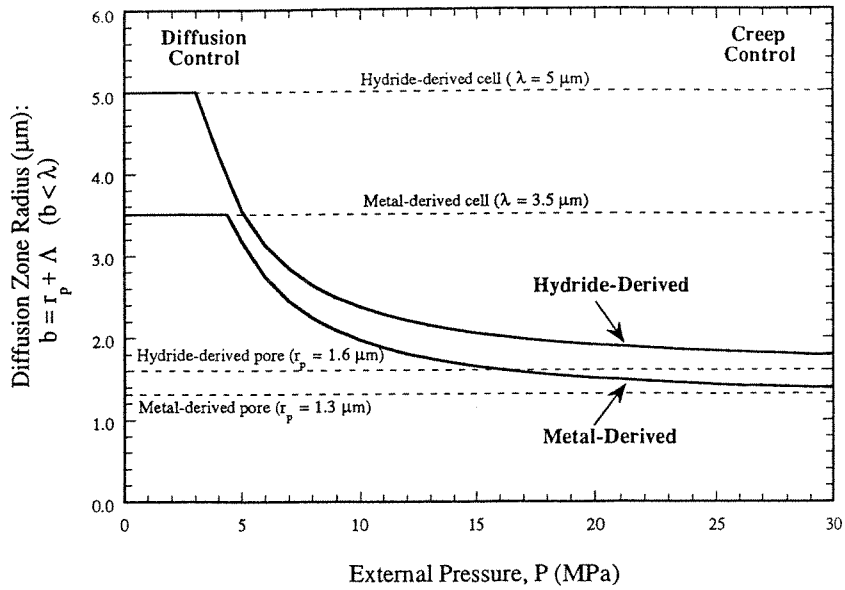

Fig. 12. Variation of diffusion zone radius with external pressure at 700°C. Also shown is relation to pore half-spacing (λ) and pore radius (r_p).

zone shrinks from $b \approx \lambda$ down to $b \approx r_p$. (Note that Hsu and Solomon [7] reported an apparent transition from $n = 1$ up to $n \approx 2$ during swelling in nickel.) The HIP results for U–10Zr were all generated between 5 and 20 MPa. If the calculated HIP rates are truncated and a linear curve fit is applied to the model between 5 and 20 MPa, the predicted n values are $n = 3.8$ and $n = 3.6$ for the hydride- and metal-derived materials, respectively, very close to the measured value of 3.7 ± 0.5.

As the transition from diffusion control to creep control occurs (i.e., boundary diffusion becomes less important and power-law creep becomes dominant), the HIP activation energy should show a similar transition. One of the physical deficiencies of the Chen–Argon model is that this transition is not evident [26]. However, our experimental measurements for Q were all made at relatively low driving forces (~ 8 MPa), where diffusion begins to become dominant (Fig. 12). This may explain why the measured activation energy consistently corresponds more closely to grain boundary diffusion. No attempts were made to measure the activation energy at higher driving forces because the HIP strain transients were too short in duration for temperature perturbation experiments.

5.3. Implications of a coupled HIP mechanism

An important implication of the coupled model is the potential for asymmetry between HIP and swelling behavior under similar conditions. Previous applications of cavitation models to HIP and swelling assumed the two processes to be reversible [7–10], which is true if they are controlled by grain boundary diffusion [10]. However, creep deformation over all, or a portion of, the grain boundary is dependent upon the stress acting upon the boundary, not upon the diffusional driving force, F. We have used the average stress on the grain boundary (Eq. (10)) to evaluate Λ, and σ_{av} is dramatically different for HIP and swelling.

Hot-isostatic pressing of the metal-derived U–10Zr with an external pressure of 20 MPa and an initial internal pressure of 1 MPa would generate an average boundary stress of ~ 21 MPa (using values for λ and r_p from Section 4.2), whereas swelling of the same material with an initial internal pressure of 20 MPa and an external pressure of 1 MPa would generate an average boundary stress less than 1 MPa. It is, therefore, feasible that HIP may be controlled by a coupled mechanism ($b < \lambda$) or even be dominated by plastic deformation because of high boundary stresses, while a reverse situation for swelling may be controlled by grain boundary diffusion ($b > \lambda$) when σ_{av} is small and Λ is large. Thus, the ability of a material to plastically deform may become much more important during HIP.

In addition, this coupled mechanism for HIP (and possibly swelling) has direct implications for metal fuel reactors and fuel performance modeling. Fuel performance codes, such as FASTGRASS [43], model the physical behavior of the fuel in the complex reactor environment. These computer models use HIP/swelling models based on a simple diffusional cavitation

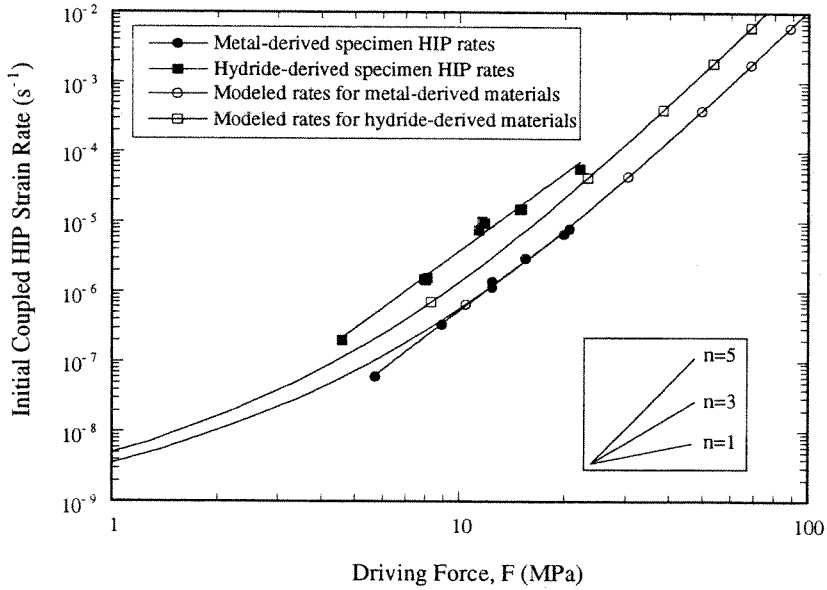

Fig. 13. Comparison of the calculated and measured initial HIP strain rates. Calculated rates determined with the coupled HIP model based on Chen and Argon [22,25].

mechanism [5] that is inconsistent with the present results for γ-phase U–10Zr of high density.

Finally, the coupled HIP model (Eq. (12)) provides some insight into possible reasons for the differences in the measured HIP rates for the hydride- and metal-derived U–10Zr specimens. The initial HIP rates for the hydride-derived specimens as a function of driving force are consistently about eight times higher than HIP rates for the metal-derived specimens (Fig. 13). The HIP rate magnitude difference for different materials may arise from variations in pore size, pore spacing, pore density on the grain boundaries, and/or the grain size; for our specimens, the only differences should be the physical differences documented in Section 4.2.

Differences in cavity density, N_v, can partially explain the difference in HIP rates, but the value of N_v for the hydride-derived material is only 1.6 times greater than N_v for the metal-derived material. In contrast, despite a strong dependence on physical parameters, the hydride- and metal-derived specimens' structure functions, $f(r_p/b)$, are nearly identical over the range of pressures used in this study (e.g., for $P = 20$ MPa and $p = 1$ MPa, $f = 0.84$ and 0.83 initially for the hydride- and metal-derived materials, respectively). In addition, the grain boundary diffusivity ($\delta_b D_b$) may also differ between the two materials because of matrix composition differences and prevalent second-phase boundaries in the hydride-derived material, but data are not available to verify that speculation.

5.4. Relevance of ex-reactor models and experiments to nuclear fuels

Despite the general acceptance of ex-reactor densification models for representing in-reactor hot-pressing [43], the question arises whether the models should be modified for in-reactor conditions, or whether unique hot-pressing mechanisms exist within the reactor. During irradiation, a supersaturation of vacancies and interstitials exists in the fuel, and this condition enhances atom mobility. However, *if* local equilibrium is maintained at the pore surfaces and grain boundary sinks, then, as argued for radiation-induced creep [44] and fission-induced densification [45], enhanced diffusion cannot affect the HIP rate since the net flux of vacancies from source to sink is unchanged and the ex-reactor models remain relevant.

However, as argued elsewhere [45], if local equilibrium at the grain boundaries cannot be maintained under irradiation as a result of the large point defect fluxes, effects of interface control may reduce the predicted rates. On the other hand, there is also the possibility that the creep component *could* be enhanced by radiation [44], causing an acceleration at high stresses and low temperatures, but no data are available on the magnitude of the radiation-enhanced creep in U–10Zr. For the outer region of the fuel, where temperatures are at or below 600°C and ex-reactor HIP was not detected, a radiation-enhanced creep component could make an important contribution in reducing fuel/clad mechanical interaction (FCMI), as it does in oxide nuclear fuels [45].

For the important case of open pores, where a pressure differential cannot exist to cause HIP, the plastic deformation of the fuel in response to FCMI becomes the dominant stress-reducing mechanism, and radiation-enhanced creep becomes crucial. The creep can occur by dislocation motion or diffusive transport, with only the former mechanism possibly enhanced by radiation.

Another effect that may be important under irradiation is the fission-fragment-induced resolution of especially small pores that may be trapped within grains. The vacancies produced by resolution may then preferentially migrate to grain boundaries under compressive stresses. As argued elsewhere [45], resolution alone is not sufficient to cause densification; the vacancies must be absorbed at the grain boundaries. Also, if the normal vacancy sources at pore surfaces, such as ledges, are poisoned by fission product 'impurities,' the pores may not be able to emit vacancies thermally, and fission-fragment-induced emission would become important.

If pores or tears in the fuel are stabilized by fission gas, then the fission-fragment-induced resolution of the gas and its motion to grain-boundary short-circuit paths for release will permit the vacancies to continue to be emitted from the pore and be absorbed at the grain boundary sinks. Thus, pressure-induced densification can continue rather than be arrested by the buildup of gas pressure within the pores.

A final effect that may be introduced during fission is enhanced diffusion in the wake of fission fragments due to intense localized heating (i.e., thermal rod). This effect was proposed to rationalize in-reactor sintering of unstable oxide fuels, where the heating is intense and of long duration in such poor conducting materials [45], but this effect may still play a role in metallic fuels at low temperatures.

The available data and models are insufficient to assess these in-reactor contributions to the HIP or densification rates, but since they generally augment the ex-reactor mechanism, the ex-reactor calculations are conservative in modeling these phenomena.

6. Summary and conclusions

For these experiments, U–10Zr specimens with closed, gas-filled porosity were fabricated from UH_3 + ZrH_2 and U + Zr powders. The hydride- and metal-

derived specimens were sintered under purified argon to entrap gas and simulate fission gas bubbles on grain boundaries. Two HIP experiments were performed at 600°C in the $\alpha + \delta$-phase field of the U–Zr alloy system. These experiments used the metal-derived specimens under HIP driving forces of 17.3 MPa. No densification was measured during either experiment, although both specimens were found to be in the metastable α'-U–10Zr phase instead of the $\alpha + \delta$-phase. This apparent incompressibility of the α'-phase at 600°C may inhibit the fuel's capability to relax fuel/cladding stresses under some conditions.

In the HIP experiments at 700°C, densification occurred with both hydride- and metal-derived specimens. In these experiments, the measured driving force dependence was found to be $n = 3.7 \pm 0.5$, and the measured activation energy was found to be 187 ± 10 kJ/mol for both types of specimens. The observed loading and unloading transients suggest that HIP is at least partially controlled by dislocation motion. Taken together, the measured values and the loading transients indicate that U–10Zr may undergo HIP by a coupled mechanism involving grain boundary diffusion and creep cavitation.

The microstructures of both types of specimens were analyzed to determine size distributions, volume fractions, and number densities for the porosity and second-phase particles. The specimen grain sizes were also measured. The majority of the pores and second-phase particles resided on the grain boundaries. These microstructural measurements are used as input parameters for the cavitation models, and the results are used in a quantitative comparison of the experimental HIP data with the theoretical models. The differences in HIP behavior between the hydride- and metal-derived samples are explained in part by differences in the pore number densities, but the magnitude of the HIP rate differences could not be fully rationalized.

In addition, it was shown that a coupled diffusion- and creep-controlled mechanism predicts an asymmetry between HIP and swelling, which has not been proposed before. Finally, it was found that a number of in-reactor phenomena could modify the ex-reactor mechanism or become important under special situations. These include radiation-enhanced creep, fission-fragment-induced resolution of small pores and fission gas atoms, localized heating, and enhanced diffusion in the wake of fission fragments.

Acknowledgement

This work was supported by the Office of Reactor Engineering, US Department of Energy, under contract no. DE-FG02-88ER12814.

References

[1] L.C. Walters, B.R. Seidel and J.H. Kittel, Nucl. Technol. 65 (1984) 202.
[2] G.L. Hofman, R.G. Pahl, C.E. Lahm and D.L. Porter, Metall. Trans. 21A (1990) 517.
[3] R.C. Abbott and A.A. Solomon, Am. Ceram. Soc. Bull. 58 (1979) 128.
[4] A.A. Solomon, K.M. Cochran and J.A. Habermeyer, J. Am. Ceram. Soc. 64 (1981) 472.
[5] A.A. Solomon, A. Casagranda and J. Rest, J. Nucl. Mater. 154 (1988) 332.
[6] A. Xu and A.A. Solomon, in: Materials Science Research, vol. 21: Microstructure of Ceramics 1986: Interfaces, eds. E.J. Pask and A.J. Evans (Plenum, New York, 1986) p. 509.
[7] F. Hsu and A.A. Solomon, Acta Metall. 31 (1983) 453.
[8] A.A. Solomon and F. Hsu, J. Am. Ceram. Soc. 63 (1981) 467.
[9] A. Xu and A.A. Solomon, J. Am. Ceram. Soc. 75 (1992) 985.
[10] A.A. Solomon and F. Hsu, in: Sintering Processes, ed. G.C. Kuczyinski (Plenum, New York, 1980) p. 485.
[11] L. Svensson and G.L. Dunlop, Int. Met. Rev. 2 (1981) 109.
[12] D. Hull and D.E. Rimmer, Philos. Mag. 4 (1959) 673.
[13] M.V. Speight and J.E. Harris, Metal Sci. J. 1 (1967) 83.
[14] J. Weertman, Scripta Metall. 7 (1973) 1129.
[15] M.V. Speight and W. Beere, Metal Sci. 9 (1975) 190.
[16] F.H. Vitovec, J. Mater. Sci. 7 (1972) 615.
[17] R. Raj and M.F. Ashby, Acta Metall. 23 (1975) 653.
[18] R. Raj, H.M. Shih and H.H. Johnson, Scripta Metall. 11 (1979) 265.
[19] W. Beere and M.V. Speight, Metal. Sci. 12 (1978) 172.
[20] D.S. Wilkinson and M.F. Ashby, Pressure Sintering by Power Law Creep, University of Cambridge Report CUED/C-Mats/TR.22 (1975).
[21] J.W. Hancock, Met. Sci. 10 (1976) 319.
[22] I.W. Chen and A.S. Argon, Acta. Metall. 29 (1981) 1759.
[23] G.H. Edward and M.F. Ashby, Acta Metall. 27 (1979) 1505.
[24] A. Needleman and J.R. Rice, Acta Metall. 28 (1980) 1315.
[25] L. Martinez and W.D. Nix, Scripta Metall. 16 (1982) 1205.
[26] J.H. Schneibel and L. Martinez, Scripta Metall. 21 (1987) 495.
[27] J.R. Rice, in: Time-Dependent Fracture of Materials at Elevated Temperature, ed. S. Wolf, US Department of Energy Report, CONF 790236 UC-25 (1979) p. 130.
[28] K. Davanas and A.A. Solomon, Acta Metall. Mater. 38 (1990) 1905.
[29] B.F. Dyson, Metals Sci. 10 (1976) 349.
[30] S.M. McDeavitt and A.A. Solomon, in: Advances in Powder Metallurgy and Particulate Materials 1992, vol. 6, Non-Ferrous Materials, eds. J.M. Capus and R.M. German (Metal Powder Industries Federation and American Powder Metallurgy Institute, Princeton, NJ, 1992) p. 109.
[31] S.M. McDeavitt, PhD thesis, Purdue University (1992).
[32] H. Lloyd and J. Williams, in: Metallurgy and Fuels, vol. 3, eds. H.M. Finniston and J.P. Howe (Pergamon, New York, 1961) p. 66.

[33] S.J. Rothman, Diffusion in Uranium and Its Alloys, Argonne National Laboratory Report ANL-5700, part C (1961).
[34] M. Hansen and K. Anderko, Constitution of Binary Alloys (McGraw–Hill, New York, 1958), p. 1250.
[35] M.I. Mendelson, J. Am. Ceram. Soc. 52 (1969) 1269.
[36] A.A. Solomon and W.D. Nix, Acta Metall. 18 (1970) 863.
[37] S.M. McDeavitt and A.A. Solomon, ANS Trans. 66 (1992) 189.
[38] M.F. Ashby, Scripta Metall. 3 (1969) 837.
[39] E. Arzt, M.F. Ashby and R.A. Verall, Acta Metall. 31 (1983) 1977.
[40] I. Kaur, W. Gust and L. Kozma, Handbood of Grain and Interphase Boundary Diffusion Data, Vol. 2 (Ziegler, Stuttgart, 1989) p. 1345.
[41] R.L. Stocker and M.F. Ashby, Scripta Metall. 7 (1973) 115.
[42] B. Derby and M.F. Ashby, Scripta Metall. 18 (1984) 1079.
[43] J. Rest, J. Nucl. Mater. 120 (1984) 195.
[44] R.V. Hesketh, J. Nucl. Mater. 35 (1970) 253.
[45] A.A. Solomon. J. Nucl. Mater. 102 (1981) 346.